Check for updates

ADVANCED MATERIALS TECHNOLOGIES
www.advmattechnol.de

Non-Planar Multiprocess Additive Manufacturing of Multifunctional Composites

*Jean-François Chauvette, Iee Lee Hia, Juliette Pierre, Gabriel Chenier, Rouhollah D. Farahani, Nicola Piccirelli, and Daniel Therriault**

Multiprocess additive manufacturing (AM) consists of integrating different 3D printing techniques to enable the fabrication of multifunctional parts, based on their geometry and material properties. The combination of fused filament fabrication (FFF) and direct ink writing (DIW) techniques, respectively involving thermoplastics and thermosetting polymers (or composites), often focuses on planar and small-scale applications (i.e., few cm), with limited nozzle orientation freedom for the fabrication of complex parts. Many industries, such as the aerospace sector, could benefit from the AM of lightweight multifunctional parts. For instance, one of the key aircraft components, the abradable seal coating, is applied on gas turbine engines casing to increase engine efficiency and is mechanically abraded by the rotor blades during engine startup. Abradable coatings made of thermosetting polymer could be 3D-printed using a multiprocess to obtain more functionalities. In this work, a non-planar multiprocess AM approach involving FFF of a complex large sandwich panel structure with low material density and large-scale DIW of an abradable thermosetting coating with controlled porosity for sound absorption potential, and better mechanical abradability than a commercial product, is presented. This multiprocess AM approach can be used to manufacture lightweight multifunctional structural parts for the automotive or aerospace industries.

1. Introduction

Multiprocess additive manufacturing (AM) is an emerging field of 3D printing research allowing the use of multiple processes or techniques in a single AM build.[1] The typical approach consists of combining different types of AM technologies, such as fused filament fabrication (FFF), stereolithography, or direct ink writing (DIW), in sequence to create a more complex final product that could not be achieved with a single process.[2,3] Multiprocess AM can lead to multifunctional devices (i.e., objects with capabilities obtained from the combination of their geometry and properties) that can range, for example, from electrical or thermal conductivity, sensing capabilities, or mechanical reinforcement.[4–8] FFF of high-temperature reinforced polymers (HTRP) is typically used to add a structural function for 3D-printed parts.[9–11] Extrusion of HTRP usually requires a high processing temperature to melt the feedstock filament (i.e., above the glass transition temperature).[12,13] On the other hand, DIW is based on the principle of continuous extrusion of a viscoelastic ink filament through a micronozzle to form a filament when the ink is coming out and is usually performed at room temperature. Its integration into a multiprocess AM build could provide complementary functionalities to the structural reinforcement of HTRP material. For example, the use of thermosetting polymers has shown potential for fire retardancy, electrostatic discharge, and sound absorption, all of which could be harnessed to manufacture multifunctional industrial parts.[14–16] In general, it is necessary to use a combination of several AM techniques when the part to be manufactured is composed of thermoplastic and thermosetting polymers (or composites).

The use of combined FFF and DIW techniques was explored by Rafiee et al. to realize the multiprocess and multimaterial AM of piezoelectric polymer (using DIW) on various thermoplastic structures (using FFF).[17] The prototypes were very small (i.e., few cm long) and the geometries were simple (e.g., beams, dome). A combination of four AM technologies (i.e., inkjet, FFF, DIW, and aerosol jetting) was demonstrated by Roach et al. to fabricate various complex multimaterial, multifunctional devices.[18] Prototypes consist, among other things, of soft pneumatic actuators and stretchable electronics that are also relatively small (i.e., not more than a few cm). This work is notable for the integration of a compact 6-axis robot (maximum arm reach

J.-F. Chauvette, I. L. Hia, J. Pierre, G. Chenier, R. D. Farahani, D. Therriault
Laboratory for Multiscale Mechanics (LM²)
Mechanical engineering department
Polytechnique Montréal
Montréal, QuébecH3T 1J4, Canada
E-mail: daniel.therriault@polymtl.ca

N. Piccirelli
Safran Paris Saclay
Centre de R&D et Bureau d'étude
Rue des jeunes bois
Chateaufort – CS80112, Magny-les-Hameaux 78114, France

The ORCID identification number(s) for the author(s) of this article can be found under https://doi.org/10.1002/admt.202300399

© 2023 The Authors. Advanced Materials Technologies published by Wiley-VCH GmbH. This is an open access article under the terms of the Creative Commons Attribution-NonCommercial License, which permits use, distribution and reproduction in any medium, provided the original work is properly cited and is not used for commercial purposes.

DOI: 10.1002/admt.202300399

of 665 mm) to perform only some pick and place operations during the process. Other researchers also reported the use of FFF and DIW for the multiprocess fabrication of tactile sensors for soft robotics, smart structures with embedded flexible sensors, multifunctional drone safety cage, and triboelectric nanogenerators.[19–22] So far, the use of thermoplastics in multiprocess AM builds has been limited to low processing temperature and relatively low-performance applications.[23] Even though, use of low-performance polylactic acid has been investigated for the FFF of a planar multifunctional (i.e., mechanical and acoustic) sandwich panel.[24] A sandwich panel is a structure made of a thick low-density core encased in thinner top and bottom skins, and is a popular structural aircraft component. The 3D-printed sandwich panel was ≈205 mm × 76 mm × 36 mm, and had a stiffness of up to ≈10% higher than that of standard hexagonal honeycomb sandwich structure. Also, by printing the panel core as Helmholtz resonators (e.g., shaped as hollow trapezoidal prisms designed for sound absorption), the sandwich panel featured a perpendicular angle sound absorption in the frequency range of ≈600 to 1200 Hz. Other authors also report the use of FFF for the fabrication of sandwich panel structures that feature a sound absorption functionality.[25–27]

In the aerospace industry, aircraft engines operate in one of the most demanding environments, where thermal expansion, misalignment, or rotation-induced stresses can cause rotating parts to rub against their casing.[28,29] To minimize the clearance between rotor blade tips and casing, sacrificial abradable coatings are applied on the casing inner surface. When the engine is running at steady state, the rotor blades extend to abrade a layer of the sacrificial coating, and the low tip clearance prevents air from leaking further into the engine, which is critical to engines efficiency and fuel economy.[29–32] Commercial thermosetting composites have been used in the industry as abradable coatings for low operating temperature regions (i.e., up to 500 °C).[33–36] Our previous work demonstrated that small-scale DIW (i.e., few cm) of a thermosetting composite has potential for producing fine abradable microscaffolds featuring sound absorption functionalities in the frequency range of 500 to 6000 Hz.[37,38] Microscaffolds are a type of micro-scale, 3D periodic filaments stacking structure (e.g., with layer orientation at 0–90°). However, scaling these particular multifunctional composite microscaffolds into actual aircraft components is a challenging task because of the usually slow printing speed and the long printing time associated with such a complex non-planar, high-resolution structure, and the need to print the actual coating on a non-planar structural aircraft component.[39,40]

Industrial 6-axis robot arms are increasingly used as AM motion system to offer the possibility of printing more complex parts with freedom of large-scale and multidirectional printing.[41,42] While 3D printing of large-scale functional industrial parts can be made possible by using 6-axis robot arms, associated printing times can be very long (e.g., up to days).[43,44] Long printing times can be overcome by multinozzle devices, which typically consist of a DIW printhead composed of several nozzles that can simultaneously extrude more than one filament.[45–47] The addition of a multinozzle printhead to a 6-axis robot arm has been shown to reduce the time it takes to print high-resolution large-scale microscaffold networks made of thermosetting polymer.[48,49]

In this work, two different AM technologies, including FFF of HTRP and multinozzle DIW of a thermosetting composite are integrated into a multiprocess AM approach using a 6-axis robot arm to demonstrate a manufacturing proof-of-concept of a large-scale non-planar complex multifunctional part. The achievement of this objective is demonstrated by manufacturing a relatively large non-planar aircraft component demonstrator, composed of a curved high-performance thermoplastic sandwich panel and a network of interconnected abradable thermosetting microscaffolds. The multifunctionality of the demonstrator is obtained by manufacturing a lightweight part, featuring the combined sound-absorption potential of Helmholtz resonators and microscaffolds, and by validating the abradable functionality of the microscaffold network in comparison to a commercially available abradable coating, referred as the benchmark.[36,50]

2. Results and Discussion

2.1. Non-Planar Multiprocess FFF of HTRP Sandwich Panel and DIW of Thermosetting Microscaffold Network

The fabrication of the aircraft component demonstrator via non-planar multiprocess FFF of an HTRP sandwich panel and multinozzle DIW of a thermosetting microscaffold network is highlighted in **Figure 1**. Figure 1a shows the three main steps of the multiprocess AM method. First, a 6-axis robot arm is setup with a custom heating enclosure and a high temperature FFF extruder to 3D print a curved HTRP sandwich panel. Specifically, the curvature of the sandwich panel conforms to the double curvature of a scanned aircraft casing topography. To reduce the risk of printing failure, the overall sandwich panel is printed in four geometrically identical sections at 15 mm s^{-1} and requires a total printing time of ≈60 h using a single nozzle of 400 µm inner diameter. Then, the panel sections are assembled together on the bottom half of the aircraft casing. The FFF extruder is unmounted from the robot flange and replaced by a 3D scanner to scan the top surface of the sandwich panel assembly and obtain a parameterized surface. The parameterized surface is then used to generate a non-planar multinozzle AM toolpath for the 6-axis robot arm (Figure S1, Supporting Information). The computed trajectory is used to guide a flow-controlled multinozzle printhead composed of 26 cylindrical nozzles of 6.5 mm long and 250 µm inner diameter, linearly spaced from center to center by 1 mm. The multinozzle printhead is used for simultaneous extrusion of a modified thermosetting composite abradable material, referred as the 0GM12FS formulation (Section S1, Supporting Information), in the shape of a microscaffold network. The thermosetting microscaffold network is 3D-printed in a non-planar layer-by-layer fashion, following the curvature of the top surface of the panel at a printing speed of 50 mm s^{-1}, and requiring ≈40 min to complete (Video S1, Supporting Information).

Figure 1b shows some of the characteristics of a printed HTRP sandwich panel section. The sandwich panel consists of a bottom skin with a thickness varying from 2–5.8 mm, a 16 mm thick core inspired by Helmholtz resonators[24,51] printed as a single extrusion wall of 0.4 mm thick, and a 12 mm thick top skin, comprising a grid infill. An analysis of the Euclidean distance between the computer-assisted drawing (CAD) model and the scan mesh of one of the printed panel sections (Figure 1c) revealed

© 2023 The Authors. Advanced Materials Technologies published by Wiley-VCH GmbH

2365709x, 2023, 17, Downloaded from https://advanced.onlinelibrary.wiley.com/doi/10.1002/admt.202300399 by Ecole Polytech De Montreal, Wiley Online Library on [07/11/2025]. See the Terms and Conditions (https://onlinelibrary.wiley.com/terms-and-conditions) on Wiley Online Library for rules of use; OA articles are governed by the applicable Creative Commons License

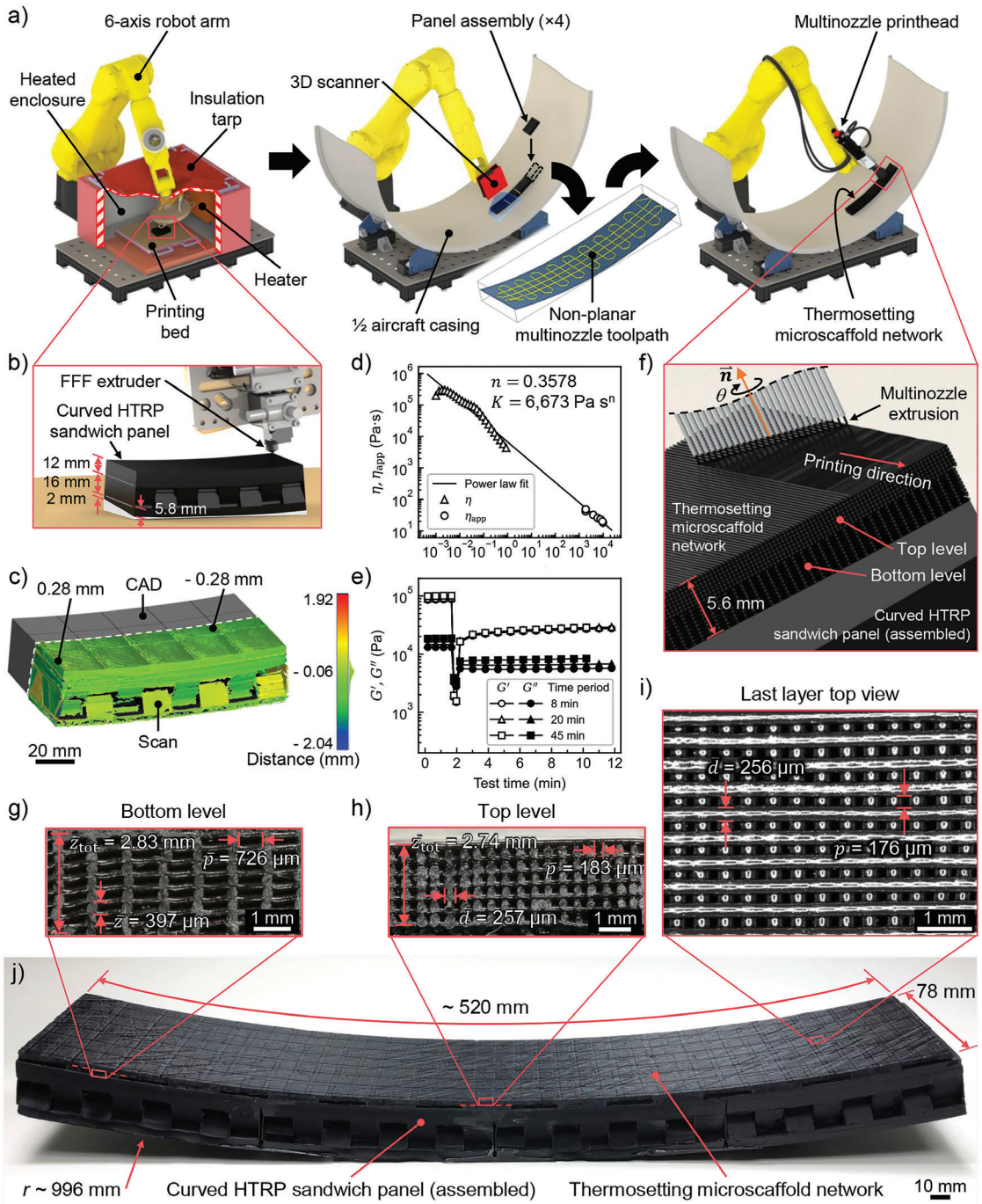

Figure 1. Non-planar multiprocess FFF of an HTRP sandwich panel and multinozzle DIW of a thermosetting microscaffold network. a) 1) FFF of curved HTRP sandwich panel using custom heated enclosure and 6-axis robot arm (the enclosure is shown with an open cross-section to see the interior), 2) HTRP sandwich panel assembly on the aircraft casing, 3D scanning of the top surface topography, and multinozzle toolpath generation, 3) non-planar multinozzle AM of abradable thermosetting microscaffold networks on top of HTRP panel assembly. b) Close-up view of FFF process and characteristics of a printed HTRP sandwich panel section, whose total thickness varies from 30 to 33.8 mm. c) Euclidean distance analysis from the comparison between CAD and scan mesh of a panel section. Max absolute error on top surface is 0.28 mm. d) Abradable material (0GM12FS formulation) shear-thinning behavior of viscosity η (obtained by rotational rheology) and process-related apparent viscosity η_{app} (obtained by capillary rheology). e) Shear storage G' and shear loss moduli G'' time-dependency of the abradable material (0GM12FS formulation) obtained from three interval thixotropy test (3iTT). f) Close-up view of multinozzle DIW process and characteristics of the printed microscaffold network, whose thickness is 5.6 mm. g) Side view on the bottom porosity level, whose thickness $\bar{z}_{tot}$ is 2.83 mm and pore size $\bar{p}$ is 726 µm. h) Side view on the top porosity level, whose $\bar{z}_{tot}$ is 2.74 mm and $\bar{p}$ is 183 µm. i) Top view on the last printed layer, where $\bar{d} = 256$ µm and $\bar{p} = 176$ µm. j) Overall view of the aircraft component demonstrator. Largest radius $r \approx 996$ mm, dimensions of the thermosetting microscaffold network is ≈520 mm × 78 mm. Overall filament diameter $\bar{d} = 257$ µm and layer stacking distance $\bar{z} = 397$ µm.

 © 2023 The Authors. Advanced Materials Technologies published by Wiley-VCH GmbH

2365709x, 2023, 17, Downloaded from https://advanced.onlinelibrary.wiley.com/doi/10.1002/admt.202300399 by Ecole Polytech De Montreal, Wiley Online Library on [07/11/2025]. See the Terms and Conditions (https://onlinelibrary.wiley.com/terms-and-conditions) on Wiley Online Library for rules of use; OA articles are governed by the applicable Creative Commons License

that the maximum absolute error of the geometric comparison is 0.80 mm (yellow), which can be explained by toolpath positioning miscalculations from our custom non-planar G-code slicing script. On the top surface, the maximum absolute error is 0.28 mm (in shades of green). The error is only 30 µm larger than the nozzles diameter of the multinozzle, which is not a problem for deposition of the thermosetting filaments.[49]

In the multinozzle process, the observed shear-thinning behavior of the 0GM12FS formulation (Figure 1d), fitted by a power law (i.e., $n = 0.3578$, $K = 6{,}673$ Pa s^n), facilitates the highly viscous material extrusion by reducing the apparent viscosity of the material η_{app} to ≈20–50 Pa s for process-related shear rates of $\dot{\gamma}_w \approx 10^3$–$10^4$ s^{-1}. The immediate recovery of shear storage modulus G' and its dominance over the shear loss modulus G'' after removal of high shear stress (Figure 1e) allow the printed thermosetting filaments to keep their shape upon extrusion for a working time of up to 45 min. Figure 1f presents a schematic of the multinozzle extrusion of the 0GM12FS formulation on top of the HTRP sandwich panel assembly. The printed thermosetting microscaffold network is 5.6 mm thick (30 layers) and is fabricated with two levels of different porosity (i.e., related to the density of printed filaments in a given space), which has been shown to be effective for broadband frequency sound absorption.[50] The first printed porosity level (i.e., bottom) is presented on Figure 1g. It is composed of layers 1–16 and has a thickness $\bar{z}_{tot}$ of 2.83 mm (standard deviation $\sigma = 0.12$ mm, mean relative error (MRE) = 11.6%). The target programmed inter-filament spacing (i.e., pore size) p on the bottom level is 750 µm and its averaged measured $\bar{p}$ is 726 µm ($\sigma = 100$ µm, MRE = 3.2%). The top porosity level (Figure 1h), is composed of layers 17–30 and has a thickness $\bar{z}_{tot}$ of 2.74 mm ($\sigma = 0.11$ mm, MRE = 2.2%). Here, the filaments are printed closer together by rotating the multinozzle printhead around its axis $\vec{\mathbf{n}}$ by an angle θ of 64.28° to obtain a target p of 184 µm. The average observed $\bar{p}$ is 183 µm ($\sigma = 36$ µm, MRE = 0.3%). On both levels' side view, the overall average vertical stacking distance for layers in the same orientation $\bar{z}$ is 397 µm ($\sigma = 49$ µm, programmed $z = 400$ µm, and MRE = 0.8%) and the overall average printed filaments diameter $\bar{d}$ is 257 µm ($\sigma = 22$ µm, theoretical $d = 250$ µm, by neglecting material swelling, and MRE = 2.8%). Overall, all dimensions show consistency with the target programmed geometry of the microscaffold network. The last layer, observed from the top view (Figure 1i), features an average $\bar{d}$ of 256 µm ($\sigma = 12$ µm, MRE = 2.4%) and $\bar{p}$ of 176 µm ($\sigma = 18$ µm, MRE = 4.1%), which is in agreement with Figure 1h.

Figure 1j shows the entire printed aircraft component demonstrator. The largest radius of the demonstrator is ≈996 mm and is located on the bottom surface of the sandwich panel which conforms to the aircraft casing curvature. On top of the panel, the curved thermosetting microscaffold network features an overall dimension of ≈520 mm × 78 mm. Using a single nozzle with the same characteristics as the multinozzle would have required more than 20 h to 3D print the same thermosetting microscaffold network with controlled porosity at the same printing speed. Such long printing time would have inevitably exceeded the working time of the 0GM12FS formulation or required a large number of material refills (estimated at ≈42 refills using 3 cm^3 syringes). The long printing times resulting from large-scale AM of thermoset composites could be overcome by mixing a latent curing agent into the material formulation.[52] Latent curing agents, such as dicyandiamide, have been shown to cause very slow reactivity at room temperature (i.e., over a week without any external thermal activation curing mechanisms).[53,54] Here, the aircraft component demonstrator exhibits the capability of the developed large-scale non-planar multiprocess method for combining high-performance thermoplastics and thermosetting composites in one AM build. The AM method successfully integrates the scaling up of a tailored thermosetting composites to obtain a 3D-printed multifunctional part, composed of high-resolution micro-scale features, printed in a relatively short time.

Table 1. Density of benchmark and parts of the aircraft component demonstrator.

Part	p [µm]	Density [g cm^{-3}]
Benchmark material	–	0.505
0GM12FS formulation	–	1.279
Bottom porosity level	750	0.346
Top porosity level	184	0.735
Overall microscaffold (both levels)	750, 184	0.535
HTRP (PEEK CF30) material	–	1.380

2.2. Multifunctionalities of 3D-Printed Aircraft Component Demonstrator

As a potential aircraft component, the 3D-printed demonstrator should be lightweight. **Table 1** presents the density of the benchmark abradable material and different parts of the manufactured aircraft component demonstrator. The 0GM12FS formulation used to 3D print the thermosetting microscaffold on top of the HTRP sandwich panel has a density of 1.279 g cm^{-3} (due to the absence of glass microspheres), which is 153% higher than that of the commercial benchmark material typically used as coating in aircraft engines (0.505 g cm^{-3}). However, the fabrication of the abradable coating as a microscaffold network with controlled porosity (i.e., $p_{bottom} = 750$ µm and $p_{top} = 184$ µm) results in an apparent density of 0.535 g cm^{-3}, which is only 5% higher than the benchmark's density. In addition, the density of the raw HTRP material is 1.380 g cm^{-3} (as provided by the manufacturer) and is approximately half that of traditional aluminum alloys (i.e., ≈2.7 g cm^{-3}) commonly used for the fabrication of aircraft casing.[55,56]

As a case study for the main functionality of the aircraft component demonstrator, the abradability of the printed thermosetting microscaffold geometry is tested by mimicking the abrasion event of aircraft engine fan blade tip during engine startup with the abradable coating. **Figure 2** presents the abradability test setup and observations of the trace left by the blade during abrasion. To comply with the experimental procedure of an in-house test rig at our industrial partner, the 0GM12FS formulation is 3D printed using a single nozzle, as a smaller planar microscaffold geometry (≈45 mm × 45 mm × 6 mm) that matches the characteristics of the top layers of the non-planar thermosetting microscaffold network printed using the multinozzle printhead (i.e., $d = 250$ µm, $p = 184$ µm, $z = 400$ µm) (Figure 2a). Figure 2b

© 2023 The Authors. Advanced Materials Technologies published by Wiley-VCH GmbH

2365709x, 2023, 17, Downloaded from https://advanced.onlinelibrary.wiley.com/doi/10.1002/admt.202300399 by Ecole Polytech De Montreal, Wiley Online Library on [07/11/2025]. See the Terms and Conditions (https://onlinelibrary.wiley.com/terms-and-conditions) on Wiley Online Library for rules of use; OA articles are governed by the applicable Creative Commons License

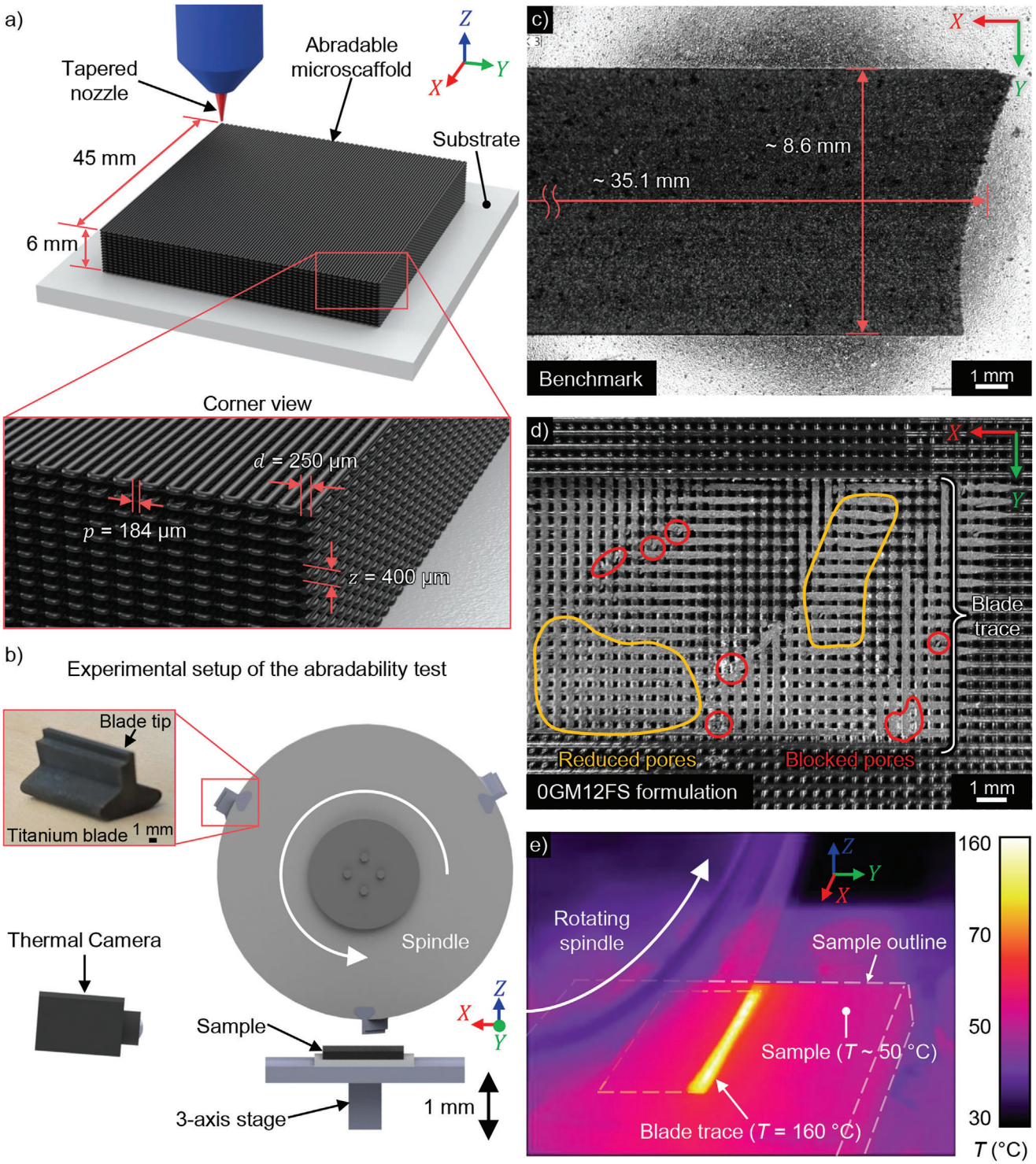

Figure 2. Abradability test setup and blade trace results. a) Schematic of a 3D-printed abradable sample made of the 0GM12FS formulation using a single nozzle (≈45 mm × 45 mm × 6 mm). b) Schematic of the abradability test rig. Three titanium blades are mounted on a rotating spindle while the abradable sample is mounted on a 3-axis stage. A thermal camera is used to record the temperature profile of the 3D-printed sample throughout the process. Once the spindle reaches the rotating speed of 15,000 rpm, the stage is moved toward the spindle at the linear speed of 0.15 mm s^{-1} and penetration depth of 1 mm. c) Microscopic top view of an abraded benchmark sample showing a blade trace of ≈8.6 mm wide and ≈35.1 mm long. d) Microscopic top view of an abraded 0GM12FS formulation sample. The blade trace shows that some pore sizes are reduced after abrasion (orange region) while some pores appear blocked (red regions). e) Side view from the thermal camera during the abradability test. The sample reached a temperature $T = 160$ °C at the location of the blade trace during abrasion.

© 2023 The Authors. Advanced Materials Technologies published by Wiley-VCH GmbH

2365709x, 2023, 17, Downloaded from https://advanced.onlinelibrary.wiley.com/doi/10.1002/admt.202300399 by Ecole Polytech De Montreal, Wiley Online Library on [07/11/2025]. See the Terms and Conditions (https://onlinelibrary.wiley.com/terms-and-conditions) on Wiley Online Library for rules of use; OA articles are governed by the applicable Creative Commons License

shows the experimental setup of the abradability test. During the test, the titanium blades rotate at 15,000 rpm, penetrate the sample following a depth setpoint of 1 mm by moving up the sample with the stage, and remove parts of the abradable material in a circular trace, while the sample temperature is recorded using a thermal camera.

Figure 2c shows the close-up top view of the blade trace on a solid molded block made of the benchmark material, which is used as a reference. The blade trace is ≈8.6 mm wide and features an average length of ≈35.1 mm. Figure 2d shows a similar top view of the blade trace on the 3D-printed sample made of 0GM12FS formulation. The blade trace is ≈8.6 mm wide and ≈36.6 mm long (dimensions not shown). It appears that some of the filaments diameter have enlarged (orange region) by ≈15% after abrasion. The sample reached a temperature of $T \approx 160$ °C (Figure 2e) in the region of the blade trace for a duration of ≈6.5 s during the test, which is higher than the glass transition temperature T_g of the 0GM12FS formulation of 45.1 °C. The rubbery state of the material at $T \approx 160$ °C can perhaps explain the enlargement of filaments, which would imply that some of its mechanical properties are reduced compared to its glassy state. The printed filament deformation hypothesis is supported by the blade—coating interaction that typically involves structural wear and a contribution from thermal effects that can result in plastic deformation and extensive flow of the coating, leading to some smearing.[57,58] The enlargement of filaments caused some of the pore sizes to be slightly reduced by ≈15% (orange region). In some cases, the pores appear to be blocked by material that was probably smeared or removed during the abrasion (red regions). It is possible that the pore size variation could alter the sound absorption functionality of the abradable thermosetting microscaffold network, as reported by some studies.[50,59]

Figure 3a shows a bar chart of the measured pore size area occupied by air with respect to the overall blade trace area from the top view, referred as percentage of open area (POA). The measurements are reported for the last layer of the 3D-printed samples before the abradability test and for the remaining abraded layers on top of the 3D-printed samples after the test. Based on the microscaffold characteristics presented in Figure 2a, the theoretical POA can be calculated using[50]

$$\mathrm{POA}_{\mathrm{theo}} = \frac{p^2}{(p+d)^2} \tag{1}$$

$\mathrm{POA}_{\mathrm{theo}}$ is found to be 18%. Before the test, the POA of the 3D-printed microscaffold was measured at $\mathrm{POA}_{\mathrm{before}} = 19\%$ ($\sigma = 1\%$) which is close to the value of $\mathrm{POA}_{\mathrm{theo}}$. After the test, the overall pore size is reduced, and it was observed that $\mathrm{POA}_{\mathrm{after}} = 16\%$ ($\sigma = 2\%$), which is caused by reduced pore size and blocked pores. Although a POA reduction of 3% (from 19% down to 16%) is observed after the test, the $\mathrm{POA}_{\mathrm{after}}$ is still in range of $\mathrm{POA}_{\mathrm{theo}}$ when adding the error bar of $\mathrm{POA}_{\mathrm{after}}$ (i.e., $\sigma = 2\%$) and should not significantly reduce the sound absorption functionality of the microscaffold network.[59,60]

Figure 3b shows a bar chart of the measured maximum blade penetration depth (i.e., the depth to which the abradable material has been removed), based on a 1 mm setpoint. The blade penetration was measured at 126% of the setpoint ($\sigma = 5\%$) for the benchmark samples and at 128% of the setpoint ($\sigma = 4\%$) for

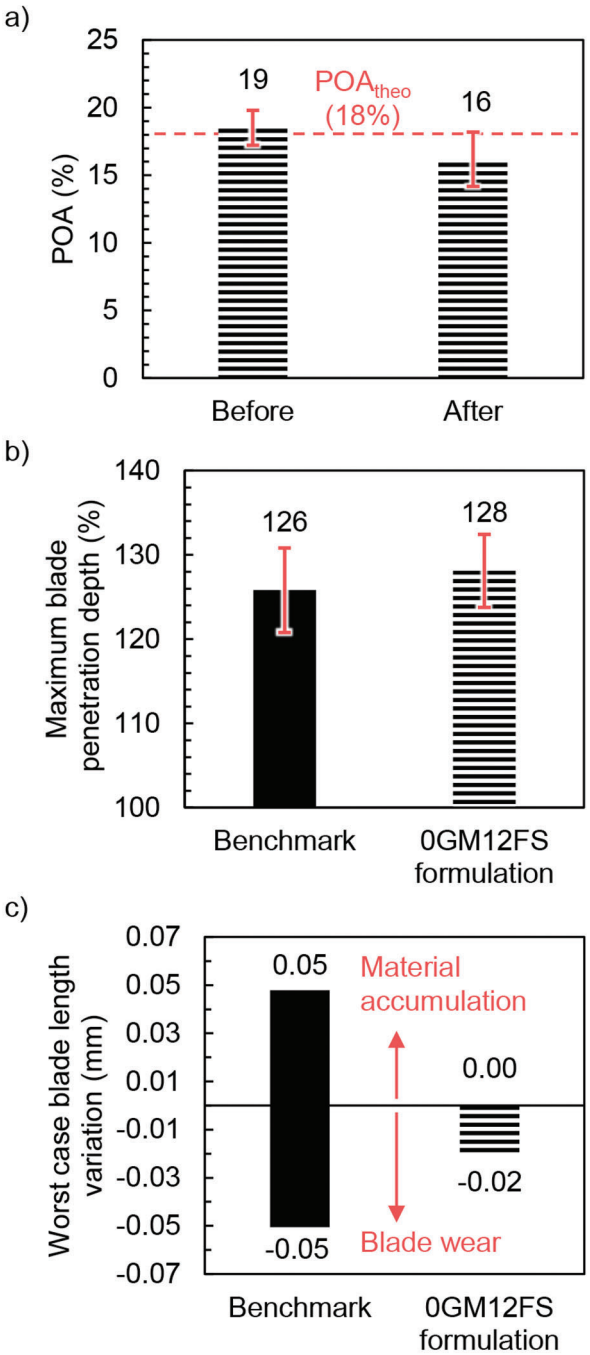

Figure 3. Analysis of abradability results between 3D-printed samples made of 0GM12FS formulation and molded samples made of benchmark material . a) Measured percentage of open area (POA) of 3D-printed sample on the last layer before the test and on the top remaining layers after the test. The theoretical POA of the printed sample is 18%. Error bars represent standard deviation ($\sigma = 1\%$ and 2%, respectively). b) Comparison of measured maximum blade penetration depth after test for benchmark and 3D-printed samples. Percentages are given with respect to the 1 mm setpoint. Error bars represent standard deviation ($\sigma = 5\%$ and 4%, respectively). c) Comparison of measured worst case blade length after test for benchmark and 0GM12FS formulation samples. Negative values represent a blade wear and positive values represent material accumulation on the blade.

© 2023 The Authors. Advanced Materials Technologies published by Wiley-VCH GmbH

2365709x, 2023, 17, Downloaded from https://advanced.onlinelibrary.wiley.com/doi/10.1002/admt.202300399 by Ecole Polytech De Montreal, Wiley Online Library on [07/11/2025]. See the Terms and Conditions (https://onlinelibrary.wiley.com/terms-and-conditions) on Wiley Online Library for rules of use; OA articles are governed by the applicable Creative Commons License

the 3D-printed samples. The proximity between the blade penetration values on both samples shows that the material removal performance of the 0GM12FS formulation is similar to the performance of the benchmark material. Although, as shown on Figure 3c, it was observed that there is a greater overall length variation of the titanium blades after abrasion of the samples made of benchmark material than after abrasion of the samples made of the 0GM12FS formulation. In some cases of samples made of benchmark, some abraded material accumulated (positive values) on the blades during the test, thus increasing the blades length by up to 0.05 mm. Some blades were also damaged (negative values), and their length was reduced by up to 0.05 mm. In the case of samples made of the 0GM12FS formulation, no significant material accumulation was observed on the blades, but some blades were worn out by 0.02 mm, which is less than for the benchmark samples. Material accumulation on actual fan blades of an aircraft engine could lead to a weight imbalance sufficient to cause damage or reduced engine performance.[33,35] On the other hand, the ejected particles that do not accumulate on the blades would be burned by the heat of the engine without causing degradation. Here, the 3D-printed abradable thermosetting microscaffolds made of the 0GM12FS formulation appear to perform better than the commercial benchmark material because of the similar blade penetration depth and a better preservation of the blades' integrity after abrasion. The abradability performance of the 0GM12FS formulation and the controlled porosity of the thermosetting microscaffold network printed on top of the HTRP sandwich panel demonstrate the ability to integrate lightweight functionalities and abrasion resistance into the 3D-printed aircraft component demonstrator.

3. Conclusion

In summary, we have developed and demonstrated a large-scale multiprocess AM proof-of-concept for fabricating geometrically complex multifunctional parts made of HTRP and thermosetting composites. The manufactured aircraft component demonstrator required the combination of FFF of HTRP and the multinozzle DIW of thermosetting composite using a 6-axis robotic arm. It was shown that the multiprocess method can 3D print a non-planar multifunctional part, composed of a reinforced sandwich panel coated with a thermosetting microscaffold network that possesses abradability and lightweight functionalities. The 3D-printed porous coating made of an abradable thermosetting microscaffold network performed better than a bulk coating made of non-printable commercial abradable material, for a similar apparent density. In addition, the combination of a sandwich panel structure inspired by Helmholtz resonators and a multilevel porosity microscaffold network could show great potential for broadband sound absorption. The reported manufactured abradable thermosetting microscaffold dimensions accounts for $1/12^{th}$ of the circumference of the casing used in this work. It is estimated that it would take ≈12 h to manufacture an abradable coating of the full circumference, which is approximately four times longer than the actual manual application method. However, it is important to note that the current application method does not allow the abradable material to be applied in the form of a microscaffold, which is an important added value to the proposed approach. The proposed multiprocess AM proof-of-concept presented in this work contributes to the large-scale integration of multifunctional materials into multiprocess AM by scaling up the DIW of thermosetting composites. Future work should focus on complete acoustic and mechanical characterization, which could lead to the manufacturing of lightweight, sound-absorbing, structural parts beneficial for the automotive or aerospace industry.

4. Experimental Section

Heated Enclosure for AM of HTRP: A custom FFF printhead device was mounted on a 6-axis robot arm (Fanuc M-20iB/25, Fanuc Canada Ltd., Canada). The device consisted of an FFF extruder (Dyze Pro, Dyze Design, Canada) installed on a high-temperature resistant machined bracket made of polyetherimide (PEI), attached to the robot mounting plate. A thick (≈10 mm) aluminum plate (≈450 mm × 450 mm) covered with polyimide adhesive film (Kapton, Dupont, USA) was used as a printing bed and was heated using a silicone rubber pad heater (SainSmart, USA). A custom heated enclosure was built for FFF of high-performance polymers in a controlled heated environment. The custom heated enclosure's floor and walls were fabricated using T-slotted aluminum extrusions and polyisocyanurate R-6 insulating panels (Atlas E148, Atlas, Canada). The printing bed was placed inside the enclosure and the top opening was isolated using an insulation tarp made of silicone (Rubber-Cal, USA), attached to the machine PEI bracket. A 3.75 kW ceramic panel (CRP20074, Omega, Canada) emitting in the infrared spectrum was used to increase the air temperature inside the enclosure and was controlled with type K thermocouples. The sandwich panel was printed using a spool of polyether ether ketone (PEEK) material reinforced with 30 wt% of carbon fibers (TECAPEEK CF30 black, Ensinger, Germany). Prior to printing, the material was dried in a vacuum oven at 60 °C for 24 h. The printing bed temperature was heated to 150 °C, the enclosure environment was heated to 110 °C and the extruder temperature was heated to 440 °C. All heaters were turned on before printing began until all temperatures stabilize.

Slicing and 3D Printing of Non-Planar HTRP Sandwich Panel: The casing surface was scanned using a 3D scanner (GOM Atos Core 200, GOM Metrology, Germany) and reconstructed as a non-uniform rational B-spline (NURBS) surface. The NURBS surface was used in a custom FFF slicer (programmed in Python) to generate a non-planar machine language for AM (G-code) that allows the FFF extruder to be aligned with the casing surface curvature. The G-code was generated using a custom non-planar variable layer height slicing method so that the first layer of the sandwich panel conforms to the curvature of the casing and the last layer of the panel conforms to a cylindrical shape whose revolution axis coincides with that of the casing.[61] Since the casing was too large to fit inside the heated enclosure, the panel was fabricated on top of conventional support material on a planar heated printing bed. The G-code for the support material was generated using Simplify 3D by a traditional planar slicing technique and added at the beginning of the sandwich panel G-code. The combined G-code was then converted to the proprietary file format for Fanuc (i.e., teach pendant programming—TPP) and launched at a printing speed of 15 mm s^{-1}. After the print, all heat sources were turned off and the printed panel was left to cool down at room temperature overnight within the open enclosure.

Characterization of Sandwich Panel: The sandwich panel sections were individually scanned using the 3D scanner and compared with the CAD model of the part. The accuracy of this HTRP FFF method was evaluated by computing the Euclidean distance between the scans and the CAD using the software CloudCompare (version 2.12.4).

Sandwich Panel Assembly: The sandwich panel sections were glued together end to end using an epoxy resin (Epon 862, Hexion, Columbus, Ohio, USA) mixed with the curing agent (Epikure 3274, Hexion, Columbus, Ohio, USA) and were left to cure for 48 h. The sandwich panel assembly was then fixed on the aircraft casing using double-sided adhesive tape (300LSE, 3M scotch, USA). Masking tape was added at the borders of

© 2023 The Authors. Advanced Materials Technologies published by Wiley-VCH GmbH

2365709x, 2023, 17, Downloaded from https://advanced.onlinelibrary.wiley.com/doi/10.1002/admt.202300399 by Ecole Polytech De Montreal, Wiley Online Library on [07/11/2025]. See the Terms and Conditions (https://onlinelibrary.wiley.com/terms-and-conditions) on Wiley Online Library for rules of use; OA articles are governed by the applicable Creative Commons License

the sandwich panel top surface to protect the panel from material losses during the multinozzle AM process.

Abradable Material Preparation: The commercial abradable material (i.e., benchmark) (Scotch-Weld EC-3524 B/A Black, 3M, France)[36] was composed of a two-part system: an amine hardener (part A) and epoxy resin (part B) which were premixed to ≈22.5 wt% of hollow glass microspheres (GM) (Glass Bubbles Floated Series, A20/1000, 3M, France). For the production of the abradability tests samples, the benchmark was prepared by mixing part A and B together (8 g per sample) at the weight ratio of 94:100 (part A:part B) using a speed mixer (FlackTek SpeedMixer DAC 330-100 SE, USA) at 2750 rpm for 30 s. The benchmark abradable material was not readily 3D printable (i.e., could not retain its printed shape after material extrusion). Thus, the abradable thermosetting 0GM12FS formulation was developed by adding up to 12 wt% hydrophobic fumed silica (FS) (CAB-O-SIL TS-720, Cabot, USA) to the neat resins (i.e., no GM content) of the commercial material, which was inspired by the previous work.[38] The 0GM12FS formulation was then prepared by mixing part A and B individually with 12 wt% of FS using the speed mixer at 2750 rpm and 30 s for three cycles. Both filled parts were then mixed together at the weight ratio of 94:100 (part A:part B) using the speed mixer at 2750 rpm for 30 s for one cycle only. For AM of an abradability test sample, the 0GM12FS formulation (3.8 g) was loaded into 3 cm^3 syringes (Nordson EFD, USA) fitted with a tapered nozzle (inner outlet diameter of 250 µm, inlet diameter of 2.7 mm, and half cone angle of 5.7°). For the AM of large-scale non-planar abradable thermosetting microscaffold networks using the multinozzle printhead, the 0GM12FS formulation (160 g total) was loaded into a 250 cm^3 reservoir fitted with a custom multinozzle array (Mëkanic—FACMO Chair collaboration, Montreal, Canada).

Material's Viscosity Measurements: Rotational shear rheology was performed using a modular compact rheometer (MCR 502, Anton Paar, Germany) fitted with a parallel plate (25 mm diameter, 1 mm gap) at 25 °C. The material's viscosity η at low shear rate was measured for $\dot{\gamma}$ ranging from 10^{-3} to 10^{0} s^{-1}. Viscosity measurements for $\dot{\gamma} > 10^{0}$ s^{-1} were excluded from the fit due to material instabilities occurring in the rheometer.[38] The material's process-related apparent viscosity η_{app} at high shear rate was measured using capillary rheology method at room temperature for process-related apparent shear rate $\dot{\gamma}_w > 10^3$ s^{-1}.[48,62] Results for η and η_{app} were fitted using a power law model $\eta = K\,\dot{\gamma}^{n-1}$.

Three Interval Thixotropy Test: The material's shear storage G' and shear loss G'' moduli's time-dependent behavior were investigated using a three interval thixotropy test (3iTT) using the rheometer at three consecutive time periods after mixing (8, 20, and 45 min).[63] The 3iTT mimicked the structural deformation and shape regeneration of the material during extrusion through the nozzles by undergoing three different oscillatory intervals.[64,65] The first interval was conducted under a low shear strain $\gamma = 0.1\%$ for 90 s, followed by a high shear strain $\gamma = 100\%$ for 19 s and back to low shear strain $\gamma = 0.1\%$ for ≈10 min. All intervals were conducted at constant angular frequency $\omega = 10$ rad s^{-1}.

Non-Planar Multinozzle Toolpath Generation: The surface of the sandwich panel assembly was scanned using the 3D scanner and reconstructed as a NURBS surface. The NURBS surface was then used to generate a non-planar multinozzle AM toolpath using the Multinozzle Toolpath Generator, a custom software based on non-planar parameterized surface projection, developed in previous work.[49] The toolpath was generated to fabricate a non-planar microscaffold network and imported in a robotic simulation software (RoboDK, version 5.4.1) to solve the inverse kinematic problem for each coordinate of the toolpath. The toolpath was then converted to TPP and imported to the 6-axis robot controller.

Multinozzle AM of Abradable Thermosetting Material: The abradable coating was fabricated as a non-planar microscaffold network using a custom multinozzle printhead (Mëkanic—FACMO Chair collaboration, Montreal, Canada) mounted on the 6-axis robot arm. Extrusion was continuous along the programmed toolpath because the printhead does not have a retraction feature, which resulted in material losses outside the microscaffold network. The multinozzle printhead was flow rate-controlled and the hydraulic pressure was automatically adjusted during all the experiment to allow the multinozzle extrusion of the 0GM12FS formulation at a printing speed of 50 mm s^{-1}. The material extrusion required a pressure gradient starting at $\Delta P \approx 9$ MPa, which increased at $\Delta P \approx 18$ MPa after 25 min of printing time, due to polymerization of the resin. Since the maximum available hydraulic pressure of the printing process was 20 MPa, the process was paused to refill the reservoir with a fresh batch of thermosetting material and was resumed to complete the print. After printing was complete, the abradable microscaffold network was left to cure at room temperature for 48 h (as reported by the manufacturer).

Characterization of Thermosetting Microscaffold Network: After the printed thermosetting microscaffold network was fully cured, material losses collected on masking tape were manually cut away using a precision cutting knife (X-ACTO, Westerville, Ohio). The microscaffold network was observed using a stereo microscope (Olympus SZX12, Olympus Corporation, Japan) and a DSLR camera (Canon EOS Rebel T4i, Canon, USA) using a macro lens (EF 100 mm 1:2.8, Canon, USA). The printed filaments diameter d, the horizontal inter-filaments spacing p (i.e., pore size), the vertical layer stacking distance z, and the porosity level thickness z_{tot} were measured using an image processing software (ImageJ, version 1.52a).

Abradability Test Samples Preparation: Six aluminum substrates (7075 T6) of dimensions 60 mm × 60 mm × 3 mm were sanded using a polisher (Metaserv 2000, Buehler, UK) with 600-grit sandpaper to remove aluminum oxide layer, followed by acetone cleaning. Samples were deposited on the substrates immediately within 2 h. For samples made of the benchmark, the prepared material was manually coated on the aluminum substrates using a silicone mold and spatula and compressed with an acetate sheet on top to achieve a flat surface. The samples were left to cure for 48 h at room temperature and the acetate sheet was removed after curing. A total of three samples were produced with dimensions of 45 mm × 45 mm × 6 mm. Samples made of the 0GM12FS formulation were 3D-printed on top of the aluminum substrates using a material extrusion dispensing system controlled by a pressure regulator (HP-7 X, Nordson EFD, USA), operated at a pressure range of 2.7–5.10 MPa to match a constant printing speed of 80 mm s^{-1}. The dispensing system was installed on a 3-axis linear stage system (Aerotech, USA) made of two planar ALS25030 stages and one vertical ALS130–100 stage, controlled via the Automation 3200 software (version 2.13). The printing parameters were set to 104 lines wide and 30 layers thick, with pore size of 184 µm for each print. A total of three 3 cm^3 syringes were required to manufacture one sample with dimension of ≈45 mm × 45 mm × 6 mm. A total of three samples were 3D-printed and subsequently left to cure at room temperature for 48 h.

Abradability Tests: The test rig (Safran Aircraft Engine, France) consists of a metal disk connected to a high-speed rotating spindle, a three-axis positioning stage, and a thermal camera (Flir A325SC, Flir, France). Three blades made of annealed titanium material were mounted on the metallic disk at a separation angle of 120°. Each abradable sample was fixed on the three-axis positioning stage, where lateral positions were adjusted so that the sample surface was within the cutting range of the blade tips. The vertical position was controlled remotely to determine the origin, where both the sample and blade tip surfaces touched each other. The initial position of the sample was set at 1 mm below the blade tip. Abradability tests began by increasing the spindle speed to 15,000 rpm gradually, associated with a blade tip velocity of ≈210 m s^{-1}. Once the desired speed was achieved, the sample was raised toward the blades at a linear speed of 0.15 mm s^{-1} with a blade penetration depth setpoint of 1 mm. After the test, the sample was returned to the initial position and the spindle was stopped.

Analysis of Abraded Samples: The abradability performance of each sample was evaluated by measuring the experimental blade penetration depth using a profilometer (ContourGT, Bruker, USA). The length of each blade was also measured using a vernier caliper, before and after the tests, to verify the blade wear and the amount of abradable material sticking to the blade. Abraded samples were then observed using a digital microscope (Keyence VH-ZST, Keyence, USA) with RZ 20–200x and 200–2000x objectives. The POA of the 3D-printed microscaffold was measured using an image processing software (ImageJ, version 1.52a) by dividing the area of pores by the total area of the abraded region from the top view on microscopic images.

Differential Scanning Calorimetry: The glass transition temperature (T_g) of abradable materials was determined from differential scanning

© 2023 The Authors. Advanced Materials Technologies published by Wiley-VCH GmbH

2365709x, 2023, 17, Downloaded from https://advanced.onlinelibrary.wiley.com/doi/10.1002/admt.202300399 by Ecole Polytech De Montreal, Wiley Online Library on [07/11/2025]. See the Terms and Conditions (https://onlinelibrary.wiley.com/terms-and-conditions) on Wiley Online Library for rules of use; OA articles are governed by the applicable Creative Commons License

calorimetry (Q1000, TA Instruments, USA) with hermetic aluminum pans and purged with nitrogen gas at 50 mL min^{-1}. Samples were prepared by weighing and mixing parts A and B manually, followed by loading into the hermetic pan and sealed immediately. Each sample was heated from −20 to 200 °C at 20 °C min^{-1}, cooled down to −20 °C at 20 °C min^{-1}, and heated again at 20 °C min^{-1} to 200 °C. Only the thermal history of the second heating cycle was useful to determine the T_g. All measurements were carried out within 5 min from the moment parts A and B were mixed.

Density Measurements: The bulk cured density of the abradable materials was measured via a helium gas pycnometer (AccuPyc II 12340, Micromeritics, USA). Cured material (≈1 g) was poured into a 3.5 cm^3 container, and placed inside the pycnometer. The densities measured were based on the average of 100 data points. The apparent densities of the printed microscaffold network were estimated by first estimating the mass of each porosity level (by multiplying the bulk cured density of the 0GM12FS formulation and the volume of printed filaments) and then dividing the obtained masses by the overall volume occupied by the microscaffold network.

Supporting Information

Supporting Information is available from the Wiley Online Library or from the author.

Acknowledgements

The authors acknowledge the financial support from the FACMO Chair supported by the Natural Sciences and Engineering Research Council of Canada (NSERC, CRDPJ 514761-1), the Canada Foundation for Innovation (CFI, Project #36450), the Government of Québec (Project #36450), and Safran Group (France). The authors also acknowledge the collaboration of Mr. Mathieu Verville for his development of the heated FFF enclosure, Mr. Dimitri Soteras for the abradability tests, Mr. Yanik Landry-Ducharme for his technical help with experimental setups, Mr. David Brzeski for his help tailoring the abradable material formulation, and the company Mëkanic for upgrades made on the multinozzle printhead.

Conflict of Interest

The authors declare no conflict of interest.

Data Availability Statement

The data that support the findings of this study are available from the corresponding author upon reasonable request.

Keywords

abradable microscaffolds, high-temperature resistant thermoplastics, material extrusion, multifunctional materials, non-planar multiprocess 3D printing

Received: March 13, 2023
Revised: April 27, 2023
Published online: June 7, 2023

[1] E. MacDonald, R. Wicker, *Science* **2016**, *353*, aaf2093.
[2] *ISO/ASTM 52900 Additive Manufacturing – General Principles – Terminology.*, ISO/ASTE International, Switzerlang, **2015**. https://www.iso.org/standard/69669.html (Accessed: September 2020).
[3] M. Rafiee, R. D. Farahani, D. Therriault, *Adv. Sci.* **2020**, *7*, 1902307.
[4] R. D. Farahani, M. Dubé, D. Therriault, *Adv. Mater.* **2016**, *28*, 5794.
[5] J. L. Coronel Jr., K. H. Fehr, D. D. Kelly, D. Espalin, R. B. Wicker, *Proc. SPIE* **2017**, *10194*, 250.
[6] S. Yang, H. Tang, C. Feng, J. Shi, J. Yang, *Micromachines* **2020**, *11*, 237.
[7] R. Tao, J. Shi, F. Granier, M. Moeini, A. Akbarzadeh, D. Therriault, *Appl. Mater. Today* **2022**, *29*, 101596.
[8] S. Khuje, A. Hehr, Z. Li, A. Krishnan, L. Kerwin, A. Kitt, J. Yu, S. Ren, *J. Mater. Eng. Perform.* **2021**, *30*, 5093.
[9] A. Diouf-Lewis, R. D. Farahani, F. Iervolino, J. Pierre, Y. Abderrafai, M. Lévesque, N. Piccirelli, D. Therriault, *Mater. Today Commun.* **2022**, *31*, 103445.
[10] B. Hu, X. Duan, Z. Xing, Z. Xu, C. Du, H. Zhou, R. Chen, B. Shan, *Mech. Mater.* **2019**, *137*, 103139.
[11] H. Jiang, P. Aihemaiti, W. Aiyiti, A. Kasimu, *Virtual Phys. Prototyping* **2022**, *17*, 138.
[12] B. G. Compton, B. K. Post, C. E. Duty, L. Love, V. Kunc, *Addit. Manuf.* **2017**, *17*, 77.
[13] C. E. Duty, V. Kunc, B. Compton, B. Post, D. Erdman, R. Smith, R. Lind, P. Lloyd, L. Love, *Rapid Prototyping J.* **2017**, *23*, 181.
[14] H. Vahabi, F. Laoutid, M. Mehrpouya, M. R. Saeb, P. Dubois, *Mater. Sci. Eng., R* **2021**, *144*, 100604.
[15] B. G. Compton, N. S. Hmeidat, R. C. Pack, M. F. Heres, J. R. Sangoro, *JOM* **2018**, *70*, 292.
[16] A. Dubourg-Cassagne, *Master's Thesis*, Polytechnique Montréal, Canada, **2015**.
[17] M. Rafiee, F. Granier, R. Tao, A. Bhérer-Constant, G. Chenier, D. Therriault, *Adv. Eng. Mater.* **2022**, *24*, 2200294.
[18] D. J. Roach, C. M. Hamel, C. K. Dunn, M. V. Johnson, X. Kuang, H. J. Qi, *Addit. Manuf.* **2019**, *29*, 100819.
[19] X. Zhou, P. S. Lee, *MRS Bull.* **2021**, *46*, 330.
[20] H. Ren, X. Yang, Z. Wang, X. Xu, R. Wang, Q. Ge, Y. Xiong, *Int. J. Smart Nano Mater.* **2022**, *13*, 447.
[21] G. L. Goh, V. Dikshit, R. Koneru, Z. K. Peh, W. Lu, G. D. Goh, W. Y. Yeong, *Int. J. Adv. Manuf. Technol.* **2022**, *120*, 2573.
[22] N. Cai, P. Sun, S. Jiang, *J. Mater. Chem. A* **2021**, *9*, 16255.
[23] N. van de Werken, H. Tekinalp, P. Khanbolouki, S. Ozcan, A. Williams, M. Tehrani, *Addit. Manuf.* **2020**, *31*, 100962.
[24] J. Pierre, F. Iervolino, R. D. Farahani, N. Piccirelli, M. Lévesque, D. Therriault, *Addit. Manuf.* **2023**, *61*, 103344.
[25] G. Szczepański, M. Podlesna, K. Lada, in *Inter-Noise and Noise-Con Congress and Conf. Proceedings*, Institute Of Noise Control Engineering, Glasgow, Scotland, **2023**, pp. 4904–4910.
[26] G. D. Goh, S. J. C. Neo, V. Dikshit, W. Y. Yeong, *J. Sandwich Struct. Mater.* **2022**, *24*, 1206.
[27] İ. Türkoğlu, M. Yazıcı, *9th International Congress on Engineering, Architecture and Design*, Bursa Uludag University, Istanbul, Turkey, **2022**, pp. 1–11.
[28] X. Ma, A. Matthews, *Surf. Coat. Technol.* **2007**, *202*, 1214.
[29] R. Rajendran, *Eng. Failure Anal.* **2012**, *26*, 355.
[30] J. Stringer, M. B. Marshall, *Wear* **2012**, *294–295*, 257.
[31] W. H. Xue, S. Y. Gao, D. L. Duan, Y. Liu, S. Li, *Wear* **2015**, *322–323*, 76.
[32] H. Ma, F. Yin, Y. Guo, X. Tai, B. Wen, *Nonlinear Dyn.*. **2016**, *84*, 437.
[33] Y.-Q. Tong, W. Li, Q.-S. Shi, L. Chen, G.-J. Yang, *J. Mater. Sci. Technol.* **2022**, *104*, 145.
[34] Y.-Q. Tong, Q.-S. Shi, M.-J. Liu, G.-R. Li, C.-J. Li, G.-J. Yang, *J. Mater. Sci. Technol.* **2021**, *69*, 129.
[35] S. Wilson, presented at The Future of Gas Turbine Technology, 6th Int. Con., Brussels, Belgium, October **2012**.
[36] 3M^{TM} Scotch-Weld^{TM} Void Filling Compound EC-3524 B/A Black, 1kg Kit, 2/cs, https://www.3m.com/3M/en_US/p/d/b40067619/ (Accessed: February 2020).

© 2023 The Authors. Advanced Materials Technologies published by Wiley-VCH GmbH

2365709x, 2023, 17, Downloaded from https://advanced.onlinelibrary.wiley.com/doi/10.1002/admt.202300399 by Ecole Polytech De Montreal, Wiley Online Library on [07/11/2025]. See the Terms and Conditions (https://onlinelibrary.wiley.com/terms-and-conditions) on Wiley Online Library for rules of use; OA articles are governed by the applicable Creative Commons License

[37] E. R. Fotsing, A. Dubourg, A. Ross, J. Mardjono, *Appl. Acoust.* **2019**, *148*, 322.
[38] D. Brzeski, I. L. Hia, J.-F. Chauvette, R. D. Farahani, N. Piccirelli, A. Ross, D. Therriault, *Addit. Manuf.* **2021**, *47*, 102245.
[39] O. Rios, W. Carter, B. Post, P. Lloyd, D. Fenn, C. Kutchko, R. Rock, K. Olson, B. Compton, *Mater. Today Commun.* **2018**, *15*, 333.
[40] B. Wang, Z. Zhang, Z. Pei, J. Qiu, S. Wang, *Adv. Compos. Hybrid Mater.* **2020**, *3*, 462.
[41] P. Urhal, A. Weightman, C. Diver, P. Bartolo, *Rob. Comput. Integr. Manuf.* **2019**, *59*, 335.
[42] P. M. Bhatt, R. K. Malhan, A. V. Shembekar, Y. J. Yoon, S. K. Gupta, *Addit. Manuf.* **2020**, *31*, 100933.
[43] A. V. Shembekar, Y. J. Yoon, A. Kanyuck, S. K. Gupta, *J. Comput. Inf. Sci. Eng.* **2019**, *19*, 031011.
[44] K. Silver, J. Potgieter, K. Arif, R. Archer, in *2017 24th Int. Conf. on Mechatronics and Machine Vision in Practice (M2VIP 2017)*, IEEE, Piscataway, NJ **2017**, pp. 1–6.
[45] C. J. Hansen, R. Saksena, D. B. Kolesky, J. J. Vericella, S. J. Kranz, G. P. Muldowney, K. T. Christensen, J. A. Lewis, *Adv. Mater.* **2013**, *25*, 96.
[46] S. J. Kranz, Master's thesis, University of Illinois at Urbana-Champaign, **2013**.
[47] M. A. Skylar-Scott, J. Mueller, C. W. Visser, J. A. Lewis, *Nature* **2019**, *575*, 330.
[48] J.-F. Chauvette, D. Brzeski, I. L. Hia, R. D. Farahani, N. Piccirelli, D. Therriault, *Addit. Manuf.* **2021**, *47*, 102294.
[49] J.-F. Chauvette, I. L. Hia, R. D. Farahani, R. Plante, N. Piccirelli, D. Therriault, *Composites, Part B* **2023**, *256*, 110627.
[50] J. Costa-Baptista, E. R. Fotsing, J. Mardjono, D. Therriault, A. Ross, *Addit. Manuf.* **2022**, *55*, 102777.
[51] F. Iervolino, *Master's Thesis*, Polytechnique Montréal, Canada, **2019**.
[52] A. M. Tomuta, X. Ramis, F. Ferrando, A. Serra, *Prog. Org. Coat.* **2012**, *74*, 59.
[53] Epoxy Curing Agents – Latent Curing Agents for One Component Systems. https://polymerinnovationblog.com/epoxy-curing-agents-latent-curing-agents-for-one-component-systems/ (Accessed: February 2023).
[54] S. D. Vacche, V. Michaud, M. Demierre, P.-E. Bourban, J.-A. E. Månson, *IOP Conf. Ser.: Mater. Sci. Eng.* **2016**, *139*, 012049.
[55] The Density of Aluminium and its Alloys – thyssenkrupp Materials (UK), https://www.thyssenkrupp-materials.co.uk/density-of-aluminium.html (Accessed: March 2023).
[56] J.-P. Immarigeon, R. T. Holt, A. K. Koul, L. Zhao, W. Wallace, J. C. Beddoes, *Mater. Charact.* **1995**, *35*, 41.
[57] M. O. Borel, A. R. Nicoll, H. W. Schla¨pfer, R. K. Schmid, *Surf. Coat. Technol.* **1989**, *39–40*, 117.
[58] F. Nyssen, N. Tableau, D. Lavazec, A. Batailly, *J. Sound Vib.* **2020**, *467*, 115040.
[59] J. Boulvert, J. Costa-Baptista, T. Cavalieri, M. Perna, E. R. Fotsing, V. Romero-García, G. Gabard, A. Ross, J. Mardjono, J.-P. Groby, *Appl. Acoust.* **2020**, *164*, 107244.
[60] W. Johnston, B. Sharma, *Addit. Manuf.* **2021**, *41*, 101984.
[61] L. Pelzer, C. Hopmann, *Addit. Manuf.* **2020**, *37*, 101697.
[62] J. Bruneaux, D. Therriault, M.-C. Heuzey, *J. Micromech. Microeng.* **2008**, *18*, 115020.
[63] 3iTT test: Anton Paar Wiki, https://wiki.anton-paar.com/ca-en/3itt-test/ (Accessed: July 2022).
[64] O. S. Toker, S. Karasu, M. T. Yilmaz, S. Karaman, *Food Res. Int.* **2015**, *70*, 125.
[65] S. G. Marapureddy, P. Hivare, A. Sharma, J. Chakraborty, S. Ghosh, S. Gupta, P. Thareja, *Carbohydr. Polym.* **2021**, *269*, 118254.

© 2023 The Authors. Advanced Materials Technologies published by Wiley-VCH GmbH

2365709x, 2023, 17, Downloaded from https://advanced.onlinelibrary.wiley.com/doi/10.1002/admt.202300399 by Ecole Polytech De Montreal, Wiley Online Library on [07/11/2025]. See the Terms and Conditions (https://onlinelibrary.wiley.com/terms-and-conditions) on Wiley Online Library for rules of use; OA articles are governed by the applicable Creative Commons License